Chemical Engineering Journal 520 (2025) 165872

Contents lists available at ScienceDirect

Chemical Engineering Journal

journal homepage: www.elsevier.com/locate/cej

A voting model weighting algorithm-driven multi-algorithm framework enhances intelligent point-of-care testing for edible oil safety

Zhiqiang Li [a,b,1], Yating Hu [a,b,1], Wen Zhang [a], Qi Zhang [a,c,d], Peiwu Li [a,c,d,e], Xiaoqian Tang [a,c,*]

[a] *Oil Crops Research Institute, Chinese Academy of Agricultural Sciences, Key Laboratory of Detection for Mycotoxin, Laboratory of Risk Assessment for Oilseed Products (Wuhan), Quality Inspection and Test Center for Oilseed Products, Key Laboratory of Biology and Genetic Improvement of Oil Crops, Ministry of Agriculture and Rural Affairs, Wuhan 430062, China*
[b] *College of Engineering, China Agricultural University, Beijing 100091, China*
[c] *Food Safety Research Institute, HuBei University, Wuhan 430062, China*
[d] *Hubei Hongshan Laboratory, Wuhan 430070, China*
[e] *Xianghu Laboratory, Hangzhou 311231, China*

ARTICLE INFO

Keywords:
Edible oil
Benzo[*a*]pyrene
Dibutyl phthalate
Metal-organic frameworks
Point-of-care testing
Intelligent analysis

ABSTRACT

Edible oils, a major source of dietary fat, are frequently contaminated with dibutyl phthalate (DBP) and benzo(*a*)pyrene (BaP), posing serious food safety risks. To enhance the accuracy of immunoassays in complex oil matrices, we developed a point-of-care testing platform that integrates bimetallic porous carbon nanomaterials as multifunctional signaling probes with a multi-algorithm framework driven by a voting model weighting algorithm. The porous carbon material Zn-CN was synthesized via organic solution coordination followed by high-temperature pyrolytic derivatization. Pt-Zn-CN was subsequently prepared by incorporating platinum nanoparticles into Zn-CN through reductive stirring at room temperature. This nanomaterial exhibits excellent photothermal properties and dispersibility, and its large surface area and porous architecture facilitate efficient antibody coupling and target enrichment. The resulting nanoprobes act as multifunctional signal transducers to enhance the recognition and amplification of antigen–antibody interactions. The multi-algorithm framework leverages bionic swarm intelligence and autonomous decision-making to perform high-precision image segmentation, attaining 97.6 % contour recognition and 95.7 % detection accuracy within 0.03 s. This platform enables ultra-fast early warning and achieves ultra-low detection limits of 0.184 ng/mL for DBP and 0.096 ng/mL for BaP. A user-friendly graphical user interface supports real-time quantification of BaP and DBP, providing intuitive safety warnings for edible oils.

1. Introduction

Edible oils are a key component of the global food system, with annual production exceeding 200 million tonnes [1]. Approximately 40 % of this total is allocated for direct human consumption [2]. As a primary source of dietary fat, edible oils provide essential fatty acids and energy [3,4]. Consequently, ensuring their safety has become a critical concern. Research has shown that PAHs and phthalates are present in nearly all edible oil samples collected worldwide [5]. Dibutyl phthalate (DBP) is a commonly used and toxic phthalate plasticizer [6]. Edible oils may become contaminated when they come into contact with plastic products containing DBP during transportation, storage, or packaging [7]. DBP exhibits significant reproductive and developmental toxicity, disrupting the human endocrine system, causing developmental deformities in the reproductive system, and increasing the risk of cancer through long-term accumulation [8,9]. Among the PAHs in edible oils, benzo[*a*]pyrene (BaP) exhibits the highest contamination rate and is the most toxic [10,11]. It is classified as a Group 1 carcinogen by the International Agency for Research on Cancer [11]. BaP is typically generated during the high-temperature processing of oilseeds, such as

---

[*] Corresponding author at: Oil Crops Research Institute, Chinese Academy of Agricultural Sciences, Key Laboratory of Detection for Mycotoxin, Laboratory of Risk Assessment for Oilseed Products (Wuhan), Quality Inspection and Test Center for Oilseed Products, Key Laboratory of Biology and Genetic Improvement of Oil Crops, Ministry of Agriculture and Rural Affairs, Wuhan 430062, China.

E-mail address: tangxiaoqian@caas.cn (X. Tang).

[1] These authors contributed equally to this work.

https://doi.org/10.1016/j.cej.2025.165872
Received 29 April 2025; Received in revised form 23 June 2025; Accepted 9 July 2025

drying, frying, and refining, leading to contamination [12]. It is carcinogenic, teratogenic, and mutagenic, with prolonged exposure resulting in immunotoxicity and reproductive toxicity [13,14]. The presence of DBP and BaP in edible oils poses a significant threat to human health.

The development of efficient, sensitive, and rapid detection methods is crucial to preventing the entry of DBP- and BaP-contaminated edible oils into the food chain. To this end, stringent regulatory standards have been established in countries such as the United States, the European Union, Japan, and China (Table S1). Point-of-care testing (POCT) technology offers a simple, rapid, and cost-effective approach [15,16], with lateral flow immunoassay (LFIA), photoelectrochemistry, and CRISPR techniques successfully applied to detect DBP and BaP in edible oils [17–20]. Although the sensitivity of most POCTs meets the requirements for on-site screening of contaminants, the complexity of edible oil matrices and the subjective nature of signal interpretation may lead to result misjudgment [21]. Therefore, the development of a user-friendly, intelligent judgment platform integrated with the detection system is essential. This platform not only provides fast and accurate results without manual interpretation but also facilitates the broader adoption and application of detection technology.

In LFIA detection, issues such as uneven distribution of signal bands and subjective errors in manual interpretation reduce detection accuracy [22]. In recent years, artificial intelligence (AI)-assisted analysis has been increasingly applied in this field, offering a promising solution to these challenges [23]. By leveraging standardized image processing techniques, AI can automate result interpretation and enhance detection accuracy [24,25]. Commonly used image processing algorithms include preprocessing techniques (e.g., noise reduction and contrast enhancement), edge detection methods (e.g., Canny's algorithm), color analysis (e.g., hue comparison and color space conversion), template matching, and morphological processing [26–28]. These methods enhance image quality, extract key features, and enable precise analysis of color band variations [29,30]. Significant advancements in image processing have been made in medical diagnostics, where these techniques have been successfully employed for qualitative and quantitative analysis of physiological indicators in saliva, body fluids, and blood [31–34]. Researchers designed a hue-recognizable LFIA using a host–guest assembly of high-color-purity semiconductor nanoplatelets. For image analysis, the incorporation of narrow-emission and color-tunable fluorescent probes enabled a gradient-based colorimetric detection scheme. This gradient-based hue change allows for precise image capture and numerical decoding via smartphones and other portable devices, thereby significantly enhancing the visualization and quantification capabilities of LFIA. This approach holds strong potential for intelligent image recognition and rapid diagnostics, particularly in home-based or resource-limited settings [35]. In addition, there's another study. Researchers have developed a dual-mode LFIA for rapid and accurate detection of chloroacetamide herbicides. The machine learning algorithm is used for image processing. By segmenting the region of interest, extracting multiple statistical features from RGB channels and establishing multiple regression models, the accurate quantification of herbicide concentration is realized, which overcomes the limitation of traditional univariate fitting that relies on manual parameter adjustment and is disturbed by the environment, and the recovery rate in corn samples reaches 85.4–109.3 %, which provides a new method for LFIA's intelligent image processing and complex matrix detection [36]. These studies underscore the potential and promise of applying image processing techniques to LFIA for the safety monitoring of edible oils. Although the aforementioned reports have proposed certain strategies to address issues such as subjectivity in examinations, difficulties in quantitative assessment, they are still constrained by challenges related to accuracy, image noise interference, and the lack of intelligent optimization of algorithm parameters.

In this study, we developed a voting model weighting algorithm (VMWA)-driven multi-algorithmic platform integrated with point-of-care testing (MAPOCT). This platform intelligently analyzes and quantifies typical contaminants, such as DBP and BaP, in edible oils, classifying the oil as either ‘safe’ or ‘warning’. To achieve multidimensional detection, we synthesized a bimetallic porous carbon material (Pt-Zn-CN) via high-temperature derivatization and metal hybridization of ZIF-8. This material was combined with a biorecognition reagent (antibody) to create a multifunctional immunodetection probe for the MAPOCT platform, which utilizes biomimetic ant colony optimization and autonomous decision-based segmentation for high-precision image segmentation and analysis. The platform dynamically adapts to variations in background and lighting conditions, ensuring stable and accurate detection performance. This study offers three key advantages: (1) The synthesized Pt-Zn-CN exhibits excellent dispersive and photothermal properties, with its large surface area and porous structure enhancing antibody adsorption and coupling. (2) The POCT simultaneously detects DBP and BaP in edible oils, achieving detection limits of 0.184 ng/mL and 0.096 ng/mL, respectively, demonstrating high sensitivity and accuracy. (3) A user-friendly, VMWA-driven multi-algorithmic platform was established, enabling multidimensional edible oil safety monitoring with AI-assisted readings.

2. Experimental section

2.1. Materials and apparatus

Anti-BaP monoclonal antibody (mAb) and anti-DBP mAb were prepared in our lab. Standard BaP, standard DBP, zinc nitrate hexahydrate, 2-methylimidazole (2-MI), sodium citrate dihydrate, hydrogen hexachloroplatinate hexahydrate, and anhydrous methanol were obtained from Aladdin Biochemical Technology Co., Ltd. (Shanghai, China). Bap-BSA and DBP-BSA conjugate were purchased from Biodragon Technology Co. (Suzhou, China). Bovine serum albumin (BSA) and polyvinylpyrrolidone (PVPK-30) were bought from Sigma-Aldrich (MO, USA). The sample pads of fusion 3 were procured from Jieyi Biotechnology Co., Ltd. (Shanghai, China). The NC membranes (FF120HP) and sample pads of fusion 5 were obtained from Whatman (Meterstone, UK). Nitrocellulose (NC) membranes of CN 95, absorbent pads, and polyvinyl chloride (PVC) substrate plates were purchased from Millipore Co. (Bedford, MA, USA). BaP and DBP solid phase extraction columns were obtained from Biocomma Technology Co. (Shenzhen, China). Unless otherwise stated, all chemicals and solvents were of analytical grade or above.

The tube muffle furnace (Kejing Co., Ltd., Hefei, China) was used to prepare the photothermal nanomaterial Zn-CN. The probe was synthesized by a high-speed freezing centrifuge (Shuoguang Electronic Technology Co., Ltd., Shanghai, China). The immunochromatographic strips were prepared from XYZ3050 dispensing platform and CM4000 guillotine cutter (BioDot, Irvine, CA, USA). Photothermal images of Pt-Zn-CN and LFIA were collected with an infrared (IR) thermal camera (FLIR Systems Inc., USA) under 808 nm laser irradiation (Taizhu Technology Co., Ltd., Shenzhen, China). The maximum absorption wavelengths were obtained by scanning antibody, Pt-Zn-CN, and immunoprobes using an ultraviolet-visible spectrophotometer (UV–Vis) (Fusion, Waltham, Massachusetts, USA). HPLC (Wukong Instrument Co., Ltd., Shandong, China) was used to detect the BaP content in cooking oil. GC–MS (Agilent Technologies Inc., USA) was used to detect the DBP content in cooking oil.

2.2. Preparation of Pt-Zn-CN

Initially, 1.013 g of Zn $(NO_3)_2 \cdot 6H_2O$ and 0.657 g of 2-MI were dissolved in 50 mL of anhydrous methanol, and the resulting solutions were mixed. The mixture was stirred at room temperature for 24 h to facilitate the crystallization of ZIF-8 [37]. The precipitate was then collected by centrifugation at 10,000 rpm for 15 min, washed six times with methanol, and dried under vacuum at 60 °C overnight. The Zn-CN composite was synthesized through high-temperature carbonization. Specifically, ZIF-8 was transferred to a tube furnace, filled with nitrogen, and heated at a rate of 2 °C/min to 800 °C. The temperature was maintained at 800 °C for 2 h before cooling, yielding the black Zn-CN product. A total of 10 mg of Zn-CN was dissolved in 10 mL of ultrapure water and dispersed via sonication. To the resulting Zn-CN dispersion, 1 mL of $Na_3C_6H_5O_7 \cdot 2H_2O$ (20 mM) and 1 mL of $H_2PtCl_6 \cdot 6H_2O$ (8 mM) were sequentially added, and the mixture was stirred for 1 h. Following this, a $NaBH_4$ solution was introduced, and stirring was continued for an additional 2 h. Upon completion of the metal ion reduction, the free metal particles were removed by rinsing the solution six times with ultrapure water.

2.3. Preparation of BaP-mAb@Pt-Zn-CN and DBP-mAb@Pt-Zn-CN probes

The probes were synthesized by mixing Anti-BaP and Anti-DBP antibodies (500 μL, 0.2 mg/mL) with Pt-Zn-CN (200 μL, 1.0 mg/mL) for 1 h at 180 rpm at room temperature. Following this, unadsorbed antibodies were removed by centrifugation at 10,000 rpm for 15 min at 4 °C. The BaP-mAb@Pt-Zn-CN and DBP-mAb@Pt-Zn-CN probes were then dispersed in 400 μL of PBS solution containing 2 % (m/v) BSA and agitated slowly for 2 h to block the remaining binding sites on the surface of the materials. After centrifugation, the probes were washed three times with deionized water, resuspended in 200 μL of PBS buffer, and stored at 4 °C.

2.4. Characterization of Pt-Zn-CN and immunoprobes

The morphology of ZIF-8, Zn-CN, and Pt-Zn-CN was characterized using a JEM-1400 flash transmission electron microscope (TEM, Hitachi, Japan) operated at an accelerating voltage of 80 kV. Elemental distribution was verified by energy-dispersive spectroscopy (EDS, Thermo Fisher, Hillsboro, CA, USA). The structural composition of Zn-CN and Pt-Zn-CN was analyzed by X-ray photoelectron spectroscopy (XPS, Thermo Fisher, Hillsboro, CA, USA), and the particle size distributions of Zn-CN and Pt-Zn-CN were measured by dynamic light scattering (DLS, Malvern, Worcestershire, UK). Field emission scanning electron microscopy (SEM, Hitachi, Japan) at 5 kV was used to characterize the BaP-mAb@Pt-Zn-CN and DBP-mAb@Pt-Zn-CN probes. Additionally, dynamic light scattering and zeta potential measurements were performed with a Mastersizer 2000 (Malvern, UK). Fourier transform infrared (FT-IR) spectra of the probes, covering a spectral range of 400–4000 cm^{-1}, were acquired on a Thermo Scientific Nicolet iS10 spectrometer (Thermo Fisher Scientific, USA).

2.5. Construction of multifunctional immunosensor

A dual-target, dual-mode lateral flow immunoassay was constructed using a base plate, NC membrane, sample pad, and absorbent pad. In brief, BaP-BSA (0.5 mg/mL), DBP-BSA (0.5 mg/mL), and goat anti-mouse IgG (1 mg/mL) were dispensed onto the NC membrane at a rate of 0.8 μL/cm to form the test line (T line) and control line (C line), respectively. The NC membrane was then dried at 37 °C for 2 h. Sample pads (Fusion 3 and Fusion 5), NC membranes (CN95, IAB120, IAB135, and FF 120 HP), and absorbent pads were sequentially assembled on a substrate (60 mm × 30 cm) with 1–3 mm overlaps. The assembled films were finally cut into 4 mm-wide strips using a guillotine cutter and stored under dry conditions for further use.

2.6. BaP and DBP detection by POCT

The assay probe mixture was prepared by dispersing 20 μL of 1.0 mg/mL BaP-mAb@Pt-Zn-CN probe and 100 μL of 1.0 mg/mL DBP-mAb@Pt-Zn-CN probe into 880 μL of flow buffer. Under optimized reaction conditions, 50 μL of BaP and DBP mixed standard solutions at varying concentrations (final concentrations of 0.1, 0.5, 5, 10, 50, 100, 500, and 1000 ng/mL) were added to the probe mixture. The test paper was then immersed in the mixture for 7 min, and bright grey lines were visually observed. Photothermal signals were captured using a thermal imager under 808 nm laser irradiation.

The colorimetric and photothermal signals were acquired using a smartphone. For quantitative analysis, the grayscale colorimetric images were converted to 8-bit grayscale images using ImageJ software. The colorimetric signal was then converted to grayscale intensity (I), and a calibration curve was generated by plotting the rate of change in grayscale intensity (y) against the concentration of BaP and DBP standard solutions (x). Standard curves of temperature change (y) versus the concentration of BaP and DBP standard solutions (x) were constructed from the collected photothermal signals. The limit of detection (LOD) for the three signals was calculated based on Eq. (1).

$$\mathrm{LOD} = 3\sigma/\mathrm{S} \tag{1}$$

S represents the slope of the standard curve; σ represents the standard deviation of 11 negative samples.

Additionally, the specificity of the POCT for BaP and DBP was evaluated by introducing homologous interferents for BaP (fluoranthene, benzo[*b*]fluoranthene, indeno[1,2,3-*cd*]pyrene, benzo[*a*]anthracene, and benzo[*k*]fluoranthene) and DBP (DMP, DEHP, DiBP, DiNP, and BBP). A 50 μL aliquot of the mixed detection probe was combined with 50 μL of interferent (final concentration of 50 ng/mL) and added to the microtiter wells. The performance was then assessed using the quantitative POCT analysis procedure described above.

2.7. Construction of VMWA-driven multi-algorithm framework

The voting model weighting algorithm begins by converting the image to grayscale and performing preliminary processing using adaptive threshold segmentation. The Ant Colony Optimization algorithm is then introduced to evaluate the effectiveness of different threshold combinations via a pheromone matrix. Based on pheromone intensity and heuristic evaluation values, the algorithm probabilistically selects among multiple parameter combinations. Each ant's parameters consist of block size and a constant (C), and through iterative optimization, the algorithm gradually refines the parameter selection to converge on the optimal threshold combination. The optimized block size and constant values are applied for adaptive threshold segmentation of the image, generating binary images and extracting image contours. The algorithm then analyzes the contours, retaining only those with the largest area. To enhance the accuracy and effectiveness of the segmented regions, the area of the smallest enclosing rectangle is used as the evaluation criterion. The Density-Based Spatial Clustering of Applications with Noise (DBSCAN) algorithm is introduced to adaptively segment the image into regions and effectively remove noise points by clustering the gradient of the image's grayscale map. After completing region segmentation and feature extraction, the algorithm further analyzes the extracted feature values using a linear regression model to obtain quantitative values for DBP and BaP. Additionally, based on the features extracted using the photothermal detection algorithm, quantitative predictions were made using the Random Forest (RF) algorithm. This paper presents a weighted voting mechanism that integrates the quantitative results from both methods. Based on the performance of the linear regression and RF models, specifically the Root Mean Square Error (RMSE) and Coefficient of Determination (R^2), the prediction results of both models are weighted to derive the optimal quantitative values for DBP and BaP. Finally, a graphical user interface is developed using Python and the Tkinter framework to facilitate interaction between the user and the system.

2.8. Sample preparation

The application of MAPOCT for the detection of real samples was demonstrated using soybean oil as a model matrix. For BaP sample preparation, 1.0 g of soybean oil was weighed, followed by the addition of 5 mL of n-hexane. Ultrasonic extraction was performed for 10 min, after which the supernatant was centrifuged at 3000 rpm for 3 min. The resulting solution was then purified using a solid-phase extraction (SPE) column to obtain the final extract for analysis. For DBP sample preparation, 1.0 g of soybean oil was weighed into a glass centrifuge tube, and 4 mL of acetonitrile along with 200 μL of n-hexane were added. Ultrasonic extraction was performed for 20 min, and the supernatant was centrifuged at 4000 rpm for 6 min. The resulting solution was purified using an SPE column to obtain the final extract for measurement.

3. Results and discussion

3.1. Preparation and characterization of Pt-Zn-CN assembly

The schematic illustrating the fabrication process of Pt-Zn-CN was presented in Fig. 1A. ZIF-8 was synthesized using the organic solution coordination method, with Zn^{2+} as the metal center and 2-MI as the organic ligand [38]. TEM revealed that ZIF-8 exhibits a smooth and uniform rhombic dodecahedral morphology with an approximate diameter of 200 nm (Fig. 2A). ZIF-8 was transformed into the porous carbon material Zn-CN through high-temperature pyrolysis derivation. This process preserved the original shape and size of ZIF-8 while rendering its surface rough and rich in pores (Fig. 2B). Pt-Zn-CN was synthesized by infiltrating and immobilizing Pt nanoparticles within the pores of Zn-CN through a simple reductive stirring process at room temperature. The incorporation of Pt nanoparticles led to a reduction in the surface roughness of Pt-Zn-CN compared to Zn-CN (Fig. 2C). Meanwhile, the synthesized Pt-Zn-CN possesses a high surface area, which facilitates enhanced antibody enrichment efficiency. To further confirm the successful assembly of Pt-Zn-CN, we conducted characterization analyses using energy-dispersive X-ray spectroscopy (EDX) and TEM-EDX elemental mapping. The results indicate that the primary

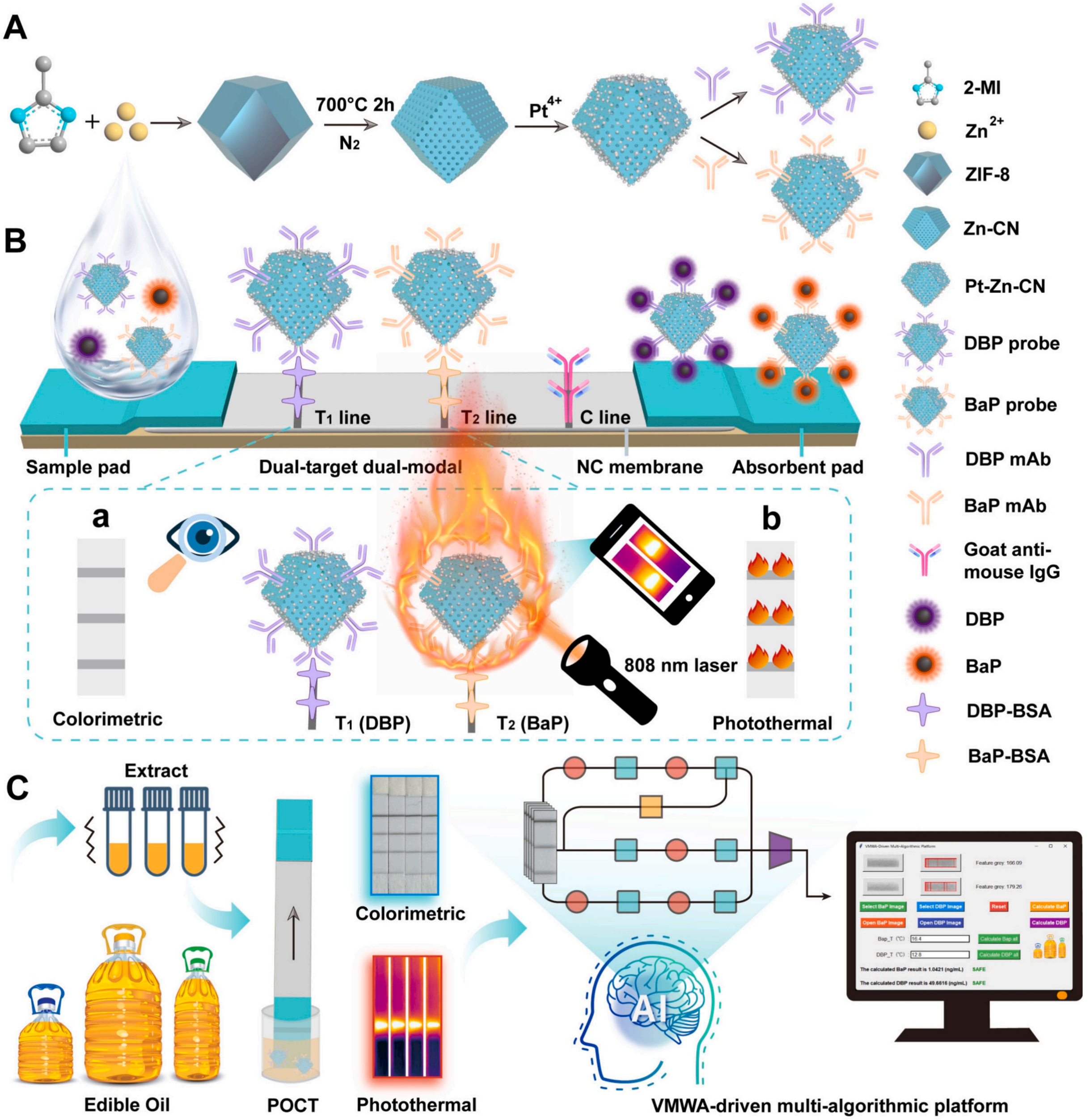

Fig. 1. Schematic illustration. (A) Synthesis of DBP and BaP probe. (B) Competitive mechanisms for multimodal analysis of DBP and BaP, (a) grey scale colorimetric signal; (b) photothermal signal. (C) MAPOCT applied to edible oil testing process.

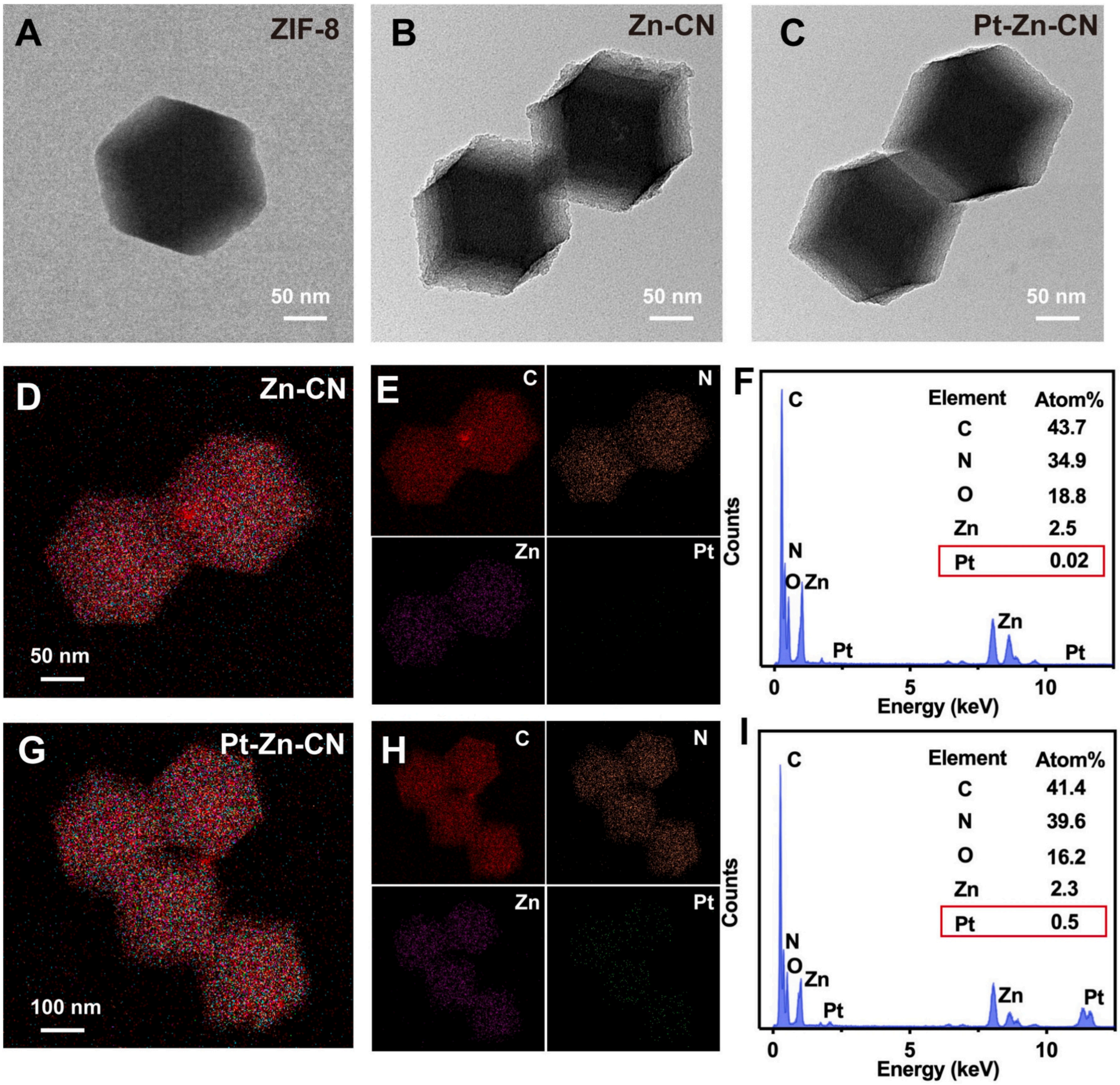

Fig. 2. Synthesis of ZIF-8, Zn-CN and Pt-Zn-CN. (A) TEM image of ZIF-8. (B) TEM image of Zn-CN. (C) TEM image of Pt-Zn-CN. (D) and (E) TEM-EDX elemental mapping of combined elements, carbon, nitrogen, zinc, and platinum of Zn-CN. (F) The corresponding EDS of Zn-CN, the atom percentage of C, N, Zn, and Pt elements. (G) and (H) TEM-EDX elemental mapping of combined elements, carbon, nitrogen, zinc, and platinum of Pt-Zn-CN. (I) The corresponding EDS of Pt-Zn-CN, the atom percentage of C, N, Zn, and Pt elements.

constituent elements of Zn-CN are C, N, O, and Zn (Fig. 2D, E, and F), with Pt detected at a level of 0.02 %. This low Pt content is attributed to interference signals generated by the interaction of the electron beam (e.g., scattered and secondary electrons) with the sample or its environment, leading to background noise in the mapping. In contrast, the main constituent elements of Pt-Zn-CN are identified as C, N, O, Zn, and Pt (Fig. 2G, H, and I), with Pt content measured at 0.5 %. This result confirms the successful synthesis of Pt-Zn-CN.

The surface morphology of the photothermal nanomaterials was examined using SEM (Fig. 3A and B). Compared to Zn-CN, Pt-Zn-CN exhibited multiple bright spots on its surface, attributed to the attachment of Pt nanoparticles. The surface chemical composition and structure of Pt-Zn-CN were analyzed using XPS. As shown in Fig. 3C, five elements (C, N, O, Zn, and Pt) were identified on the surface of Pt-Zn-CN, consistent with the results obtained from EDS analysis. High-resolution XPS was used to characterize the C 1s, Pt 4f, N 1s, and Zn 2p spectra of Pt-Zn-CN. The C 1s spectrum was deconvoluted into four distinct peaks at 284.04 eV, 284.80 eV, 286.23 eV, and 288.09 eV, corresponding to C=C, C—C, C—O, and C=O bonds, respectively (Fig. 3D). The Pt 4f spectrum was deconvoluted into two characteristic peaks at 70.86 eV and 74.54 eV, corresponding to Pt0 $4f_{7/2}$ and Pt0 $4f_{5/2}$, respectively (Fig. 3E). In addition, the N 1 s and Zn 2p spectra were deconvoluted into three and two distinct peaks, respectively (Fig. S1). The water solubility and dispersibility of Pt-Zn-CN were evaluated. In its dry state, Pt-Zn-CN appeared as a black powder. Upon dissolving in ultrapure water and undergoing sonication for 5 min, it dispersed uniformly in water (Fig. 3F). The particle size of Pt-Zn-CN in water was slightly larger than that of Zn-CN (Fig. 3G). Moreover, the zeta potential of Pt-Zn-CN was higher than that of Zn-CN (Fig. 3H), with the increased zeta potential indicating improved dispersion of the solution. This enhanced aqueous dispersibility of Pt-Zn-CN was attributed to the assembly of Pt on the surface, which altered the surface charge distribution and increased electrostatic repulsion between particles. The good dispersion of Pt-Zn-CN is more beneficial for the synthesis of immunodetection probes and the chromatography of lateral flow immunodetection.

3.2. *Photothermal properties of Pt-Zn-CN assembly*

As shown in Fig. S2, Pt-Zn-CN has the potential to perform efficient photothermal conversion. To evaluate the photothermal properties of

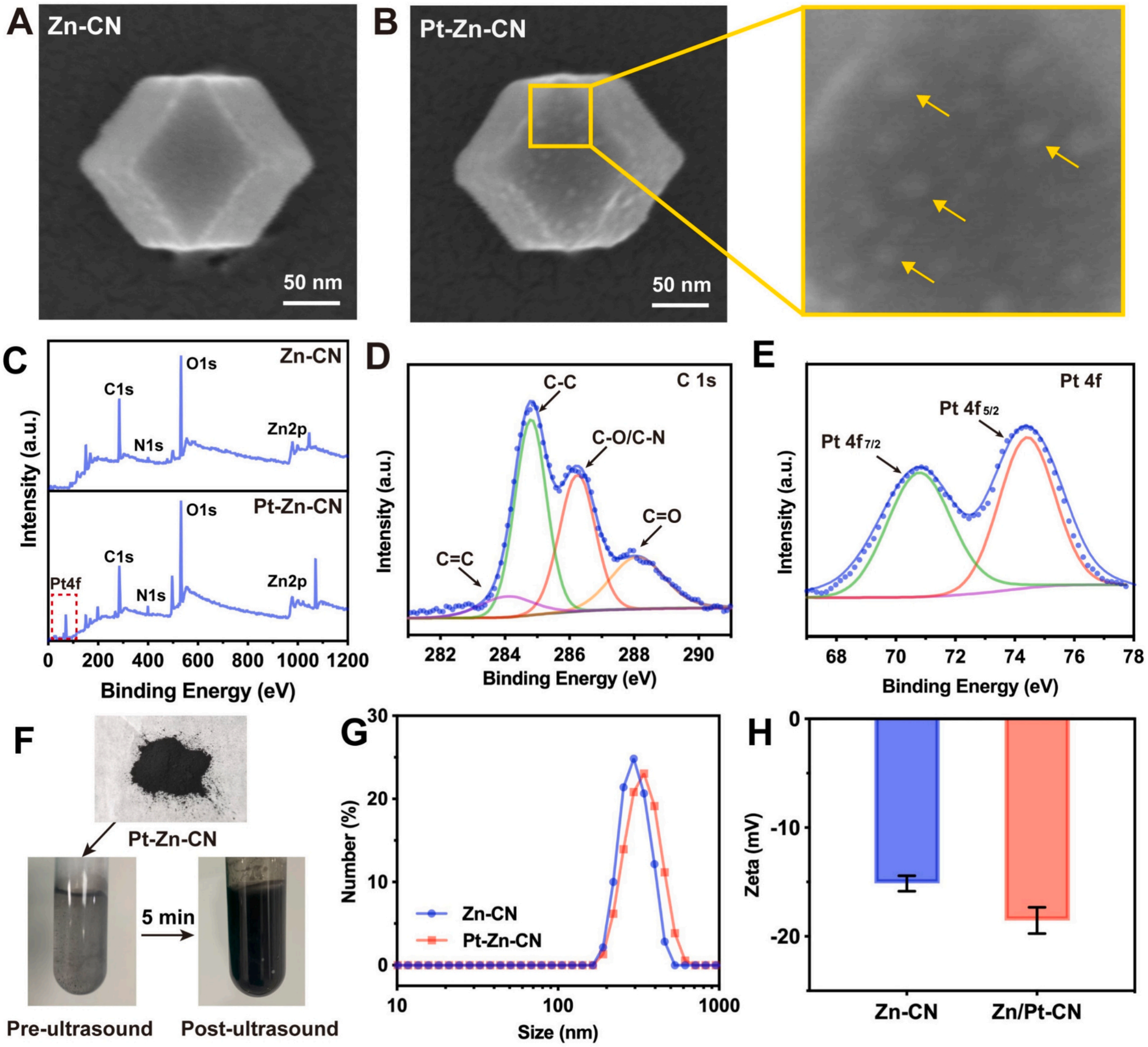

Fig. 3. Characterization analysis of Pt-Zn-CN. (A) SEM image of Zn-CN. (B) SEM image of Pt-Zn-CN. (C) Survey XPS spectra of Zn-CN and Pt-Zn-CN. C 1s (D) and Pt 4f (E) spectra of Pt-Zn-CN. (F) Pt-Zn-CN aqueous solution before and after sonication. (G) DLS and (H) Zeta potential of Zn-CN and Pt-Zn-CN. Error bars represent the standard deviation from three independent experiments.

Pt-Zn-CN, the solution was irradiated with an 808 nm laser, resulting in a gradual temperature increase with prolonged excitation time (Fig. 4A). Notably, the photothermal response temperature of Pt-Zn-CN exceeded that of Zn-CN by >10 °C under identical excitation conditions (Fig. 4B), demonstrating a significant enhancement in its photothermal performance. This enhancement is attributed to the incorporation of metallic platinum particles, which amplify the surface plasmon effect, minimize energy losses during non-radiative transitions, and significantly improve the photothermal conversion efficiency [39]. The photothermal mechanism of Pt-Zn-CN is illustrated in Fig. 4C. Upon NIR irradiation, electrons in the valence band of Pt-Zn-CN absorb energy and are excited to the conduction band, forming electron-hole pairs. These excited electrons subsequently undergo non-radiative transitions, releasing energy as heat, and ultimately return to the ground state, completing the photothermal conversion process [40,41]. As shown in Fig. 4D, the photothermal response temperature of the Pt-Zn-CN solution increases with both rising concentration and prolonged irradiation time. Under varying NIR laser power levels, a higher laser power result in a more pronounced photothermal effect (Fig. 4E). Whereafter, the thermal stability of Pt-Zn-CN was evaluated through three cycles of laser irradiation (Fig. 4F). Throughout the three photothermal cycles, the temperature remained stable, demonstrating the excellent photothermal stability of Pt-Zn-CN.

3.3. Demonstration of the integrated DBP-mAb@Pt-Zn-CN probe and BaP-mAb@Pt-Zn-CN probe

The DBP-mAb@Pt-Zn-CN probe (DBP probe) and BaP-mAb@Pt-Zn-CN probe (BaP probe) were synthesized via electrostatic adsorption coupling for the development of a dual-modal immunosensing platform designed for the detection of DBP and BaP in edible oils. The two immunodetection probes were well dispersed in PBS (Fig. S3). SEM imaging of DBP and BaP probes revealed a pseudo-spherical protruding antibody film attached to the probe surface (Fig. 5A and B). UV–Vis spectroscopy analysis (Fig. 5C) revealed that the DBP and BaP probes exhibited characteristic absorption peaks at 210 nm and 280 nm, corresponding to the peptide bond and tryptophan, respectively. The absorption spectrum of the Pt-Zn-CN solution remained stable at 0.7 a.u., which can be attributed to the black color of the solution, which absorbs both visible and ultraviolet light. Both probes displayed the characteristic absorption peaks of the antibody, and the absorbance remained above 0.7 a.u., indicating successful loading of the antibody onto the surface of Pt-Zn-CN. The probes were characterized using FT-IR

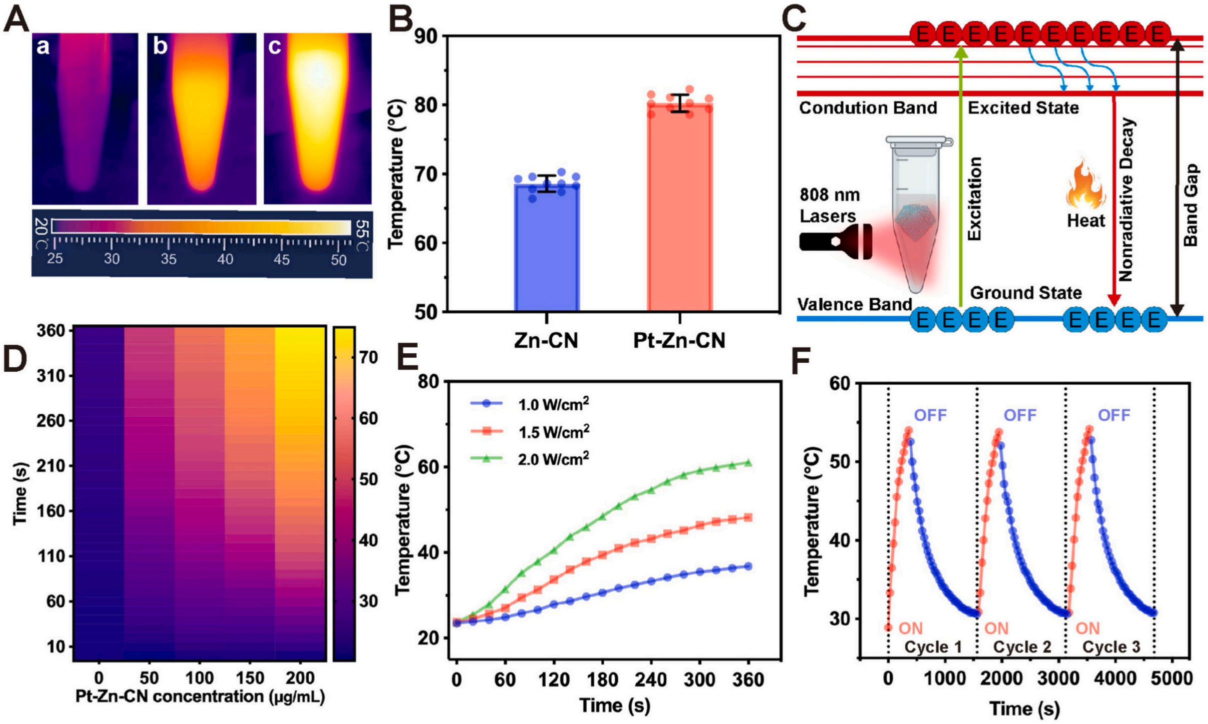

Fig. 4. Photothermal performance analysis of Pt-Zn-CN. (A) The corresponding thermographic images of Pt-Zn-CN (100 μg/mL) for (a) 0 min, (b) 3 min, and (c) 5 min (808 nm, 2.0 W/cm^2). (B) Comparison of photothermal performance of Zn-CN and Pt-Zn-CN (200 μg/mL, 808 nm, 2.0 W/cm^2, 6 min). (C) Mechanism for the photothermal performance of Pt-Zn-CN. (D) Thermograms for different concentrations and excitation times of Pt-Zn-CN. (E) Heat curve of Pt-Zn-CN solution (100 μg/mL) under 808 nm laser with different laser densities. (F) Temperature variation of Pt-Zn-CN solution during three laser irradiation cycles.

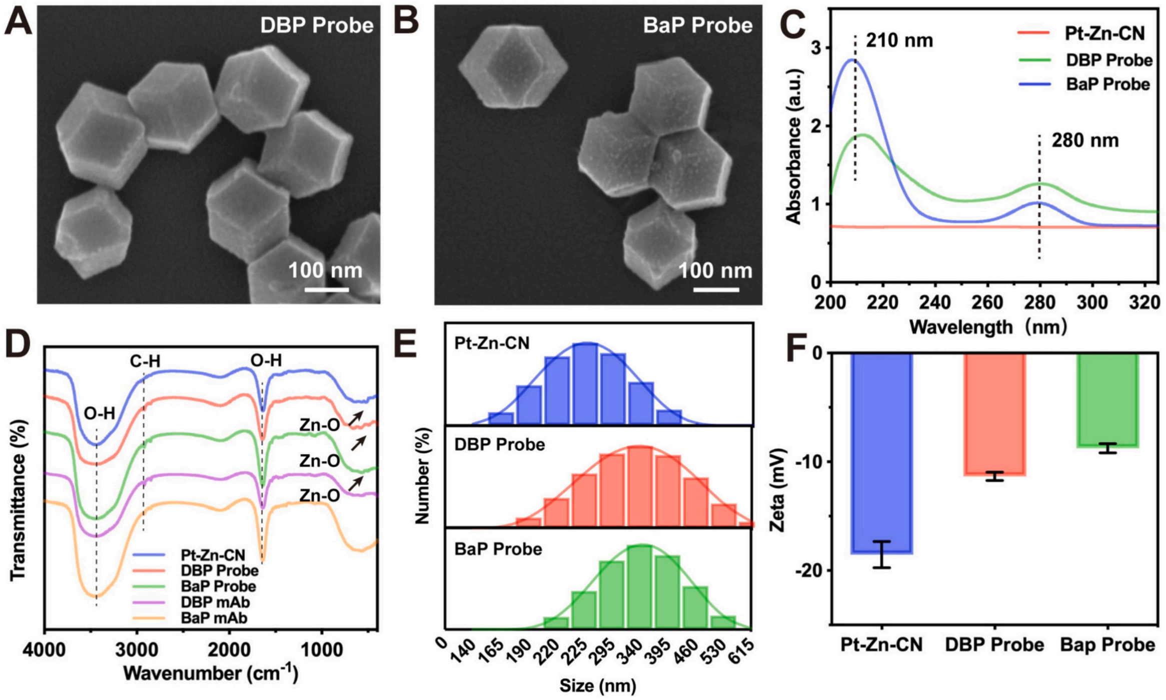

Fig. 5. Characterization of DBP-mAb@Pt-Zn-CN probe and BaP-mAb@Pt-Zn-CN probe. (A) SEM image of DBP probe. (B) SEM image of BaP probe. (C) UV–Vis absorption spectra of Pt-Zn-CN, DBP probe, and BaP probe. (D) FT-IR spectra of Pt-Zn-CN, DBP probe, BaP probe, DBP mAb, and BaP mAb. (E) DLS and (F) Zeta potential of Pt-Zn-CN, DBP probe, and BaP probe. Error bars represent the standard deviation from three independent experiments.

spectroscopy (Fig. 5D). The three peaks observed at 3450 cm^{-1}, 2920 cm^{-1}, and 1630 cm^{-1} corresponded to the O—H stretching vibration, C—H stretching vibration, and O—H bending vibration due to hydrogen bonding, respectively. Additionally, the Zn—O vibrational absorption peak at 510 cm^{-1} for both probes was identical to that of Pt-Zn-CN, confirming the success of the coupling. As shown in Fig. 5E, the particle sizes of both probes were larger than that of Pt-Zn-CN, which can be attributed to the increase in hydrated particle size resulting from the attachment of antibodies to the surface of the material. Zeta potential analysis was performed to assess the change in surface charge of Pt-Zn-CN and the probes. As shown in Fig. 5F, the zeta potentials of the DBP probe (−11.33 mV) and BaP probe (−8.75 mV) were significantly altered compared to the negatively charged Pt-Zn-CN (−18.53 mV), due to the introduction of the positively charged DBP mAb and BaP mAb.

3.4. The principle of POCT-mediated multifunctional sensing platform

As shown in Fig. 1B, the POCT platform for the detection of DBP and BaP in edible oils consists of an absorbent pad, a sample pad, a NC membrane, and a substrate. NC membranes pretreated with DBP-BSA, BaP-BSA, and goat anti-mouse IgG were employed as the T_1, T_2, and control lines for probe capture. The DBP probe and BaP probe served as signal labels, enabling both colorimetric and photothermal readings. As the probes traverse the POCT strip, the DBP probe specifically binds to DBP-BSA on the T_1 line, forming an immune complex, while the BaP probe specifically binds to BaP-BSA on the T_2 line. The remaining unbound probes continue moving and bind to goat anti-mouse IgG immobilized on the control line. Thus, the immune complexes on the test line exhibited characteristic grey areas, and the chromatic signal of the test line was further enhanced over time. In the presence of DBP and BaP in the buffer system, DBP and DBP-BSA compete as antigens for the DBP probe, while BaP and BaP-BSA compete for the BaP probe. As the levels of DBP and BaP increase, fewer probes bind to the detection line, resulting in lighter chromaticity of the strips. This allows for both quantitative and qualitative detection through colorimetry. Attractively, the two detection probes exhibit excellent photothermal properties, and their photothermal signals can serve as supplementary indicators for the quantification of DBP and BaP. Overall, POCT offers a valuable and versatile platform for the detection of plasticizers and benzopyrene in edible oils.

3.5. Optimization of POCT-based sensing performance

The sensing performance of the POCT was optimized based on grey scale intensity, band definition and background interference. Among them, the optimal sample pad was Fusion 3 (Fig. S4) and the optimal NC film was 90-2A (Fig. S5). The composition of the buffer significantly influences the reaction efficiency, signal intensity, and sensitivity during the chromatographic process. Five different buffer formulations with varying compositions were designed (Table S2). Among them, the optimal buffer composition was determined to be 1 % PVPK-30, 1 % sucrose, 1 % BSA, 1 % Tween 20, and PBS (Fig. 6A). The concentration of the probe is directly proportional to the signal strength of the detection line (Fig. 6B); however, excessive probe concentration can reduce detection sensitivity. Therefore, the optimal working concentrations for the DBP and BaP probes were determined to be 50 μg/mL and 10 μg/mL, respectively, to ensure stable POCT signal output. In a reaction system with a total volume of 100 μL, the optimal methanol concentration was found to be 30 % (Fig. 6C). The chromatography time of POCT was optimized (Fig. 6D), with the signal intensity of the test line reaching saturation at 7 min. Thus, the optimal chromatography time was determined to be 7 min. Notably, the photothermal temperature of the test line increased with the 808 nm laser irradiation time (Fig. 6E), rising sharply and reaching saturation within 30 s. Therefore, the optimal IR irradiation time was found to be 30 s. The specificity of POCT for detecting DBP and BaP within the same system was evaluated (Fig. 6F). When the system contained only the BaP probe, BaP specifically bound to the T_2 detection line but not to T_1. Conversely, in the presence of only the DBP probe, binding occurred exclusively at T_1. These results demonstrate that POCT can independently detect DBP and BaP with high specificity and without cross-reactivity.

3.6. The POCT assay for DBP and BaP

The sensing performance of the POCT for detecting DBP and BaP was

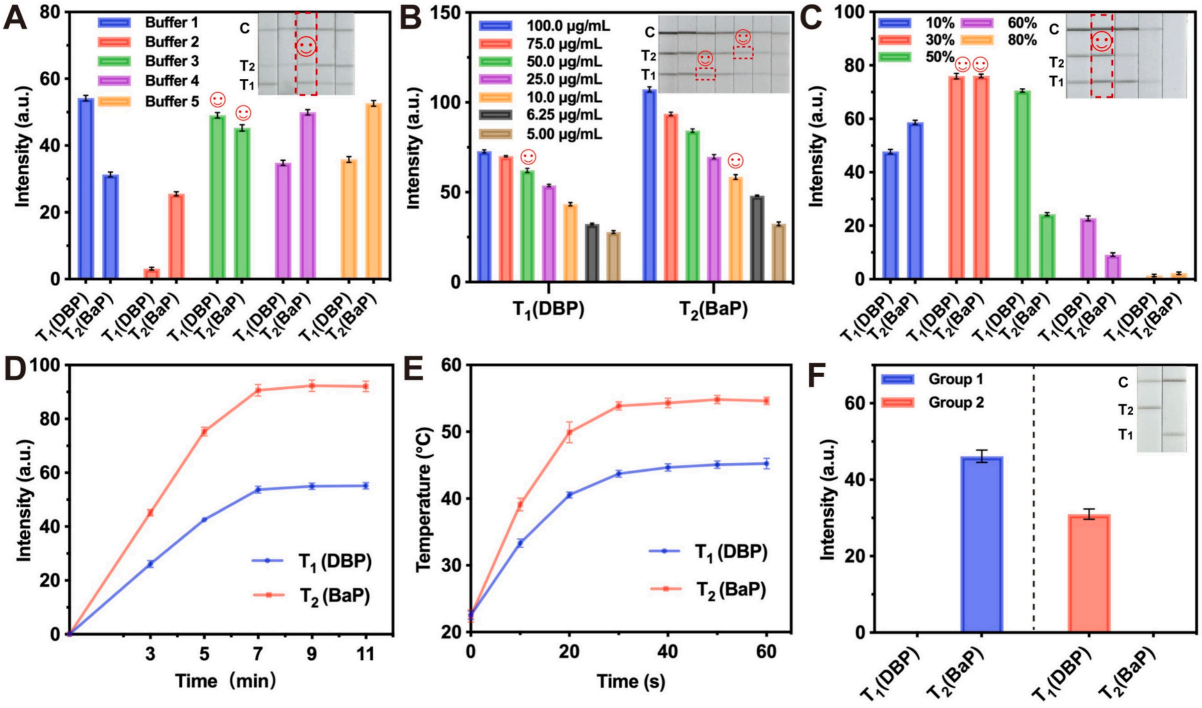

Fig. 6. Optimization of key parameters of the POCT. (A) The probe buffer diluent recipe optimization. (B) Optimization of probe content. (C) Optimization of methanol content. (D) Optimizing probe chromatography time. (E) The optimization of NIR laser irradiation detection time. (F) Reciprocal interference experiments for DBP and BaP assays (Group 1: Contains only BaP probes; Group 2: Contains only DBP probes). Error bars represent the standard deviation from three independent experiments.

evaluated under the optimized conditions described previously. This method analyzes various concentrations of DBP and BaP by measuring both colorimetric and photothermal signals. Fig. 7A illustrates the relationship between colorimetric signal intensity (I) and DBP concentration (0.5–1000 ng/mL). The regression equation is $Y = 103.0–14.04\times$, with a correlation coefficient of $R^2 = 0.9859$ (inset of Fig. 7A). The limit of detection (LOD) for DBP, determined using 11 negative sample sets (Fig. S6A), was calculated to be 0.184 ng/mL based on the formula LOD = 3σ/S. The strips were excited by 808 nm laser light, and a standard curve was established by acquiring photothermal signals through smartphone thermal imaging. The linear relationship between ΔT and DBP concentration (1–1000 ng/mL) was established using the regression eq. $Y = 20.15–5.793\times$ ($R^2 = 0.9681$) (Fig. 7B), with a LOD of 0.252 ng/mL (Fig. S6B). Similarly, the linear relationship between the grey intensity and the concentrations of BaP (0.25–300 ng/mL) under colorimetric signals is described by the regression eq. $Y = 92.39–13.83\times$ ($R^2 = 0.9812$) (Fig. 7C), with a LOD of 0.096 ng/mL (Fig. S6A). A linear relationship between ΔT and BaP concentrations (0.5–300 ng/mL) was established, described by the regression eq. $Y = 14.2–4.814\times$ (Fig. 7D), with a correlation coefficient of $R^2 = 0.9773$ and a LOD of 0.26 ng/mL (Fig. S6B). The POCT was also highly selective and reliably quantitative at significantly different concentrations (Fig. S7), with no significant cross-talk between detection zones. Compared to recently reported DBP and BaP assays (Table S3), this work offers high sensitivity, a wide detection range, and an overall detection time of only 7.5 min. Furthermore, this approach enables the simultaneous detection of both DBP and BaP and can be integrated with intelligent analytical algorithms for rapid prediction and interpretation of results. This improvement is attributed to the photothermal nanomaterial Pt-Zn-CN, which efficiently enriches antibodies and possesses excellent photothermal properties, effectively enhancing both colorimetric and photothermal signal outputs. Additionally, specificity is a critical parameter in evaluating the performance of the POCT sensing platform. During the assay, DBP and BaP showed no significant cross-reactivity with the structural analogues and exhibited good specificity (Fig. S8). We evaluated the stability of the test strips, which were stored in a room-temperature drying cabinet for 0, 20, 40, and 60 days. The contrast color and thermal signals were compared under identical detection conditions. The results (Fig. S9) demonstrated that there was no significant change in either signal after 60 days of storage, indicating that the immunosensor exhibits good stability.

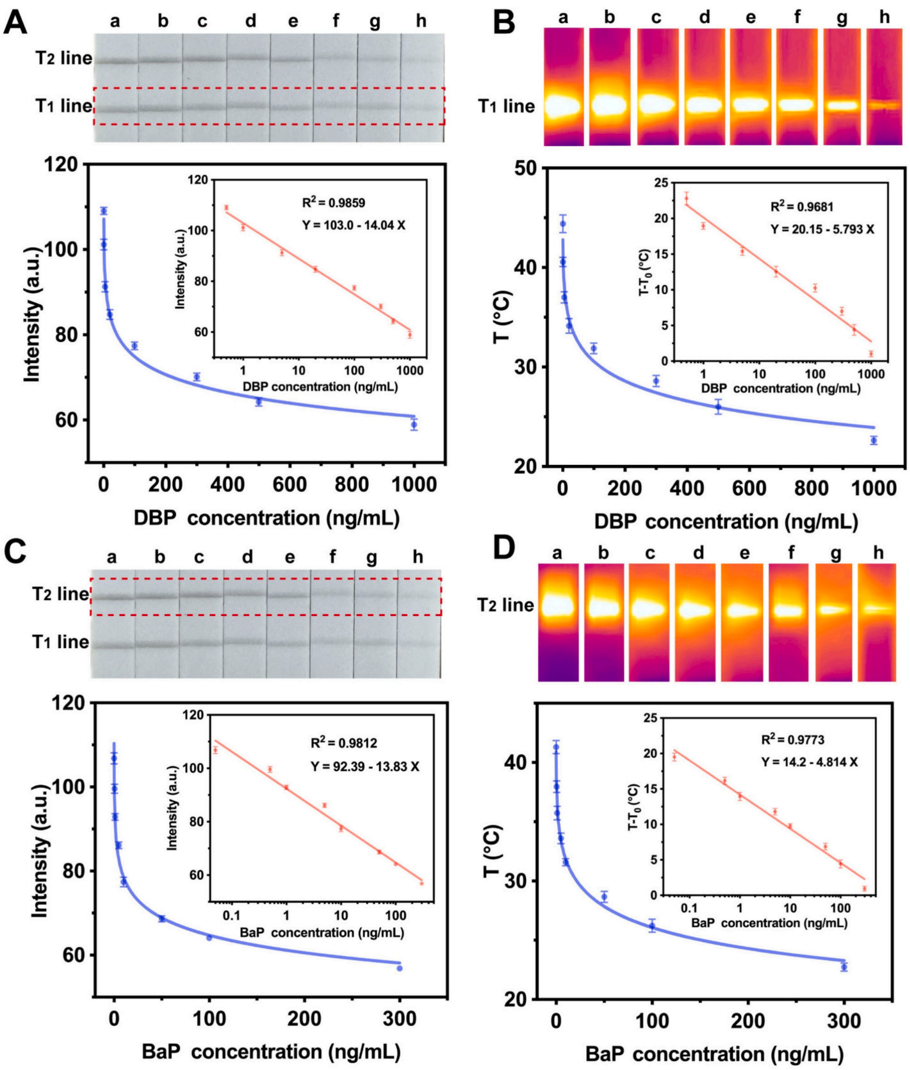

Fig. 7. Dual-modal signal output analysis of DBP and BaP. (A) Colorimetric detection of DBP (a-h DBP concentration (ng/mL) were: 0.5, 1, 5, 20, 100, 300, 500, 1000), inset: linear relationship between concentration and intensity ratio of DBP. (B) Temperature response assay for DBP, inset: linear relationship between the concentration of DBP and the temperature difference ratio. (C) Colorimetric detection of BaP (a-h BaP concentration (ng/mL) were: 0.05, 0.5, 1, 5, 10, 50, 100, 300), inset: linear relationship between concentration and intensity ratio of BaP. (D) Temperature response assay for BaP, inset: linear relationship between the concentration of BaP and the temperature difference ratio.

3.7. Multi-algorithm for quantitative analysis of DBP and BaP

Aiming at the pain points such as uneven grey scale of POCT test strips and difficulties in end-user interpretation, this study innovatively develops an intelligent diagnostic platform based on multimodal information fusion with VMWA (Fig. 8A), which achieves accurate prediction of BaP and DBP concentrations in edible oil and risk determination through the synergistic effect of bionic population intelligent optimization algorithms and autonomous decision-making segmentation (Fig. S10). The software classifies the result as ‘safe’ when the DBP concentration in edible oil is ≤0.3 mg/kg; otherwise, it is classified as ‘warning’. Similarly, when the BaP concentration is ≤10 μg/kg, the result is considered ‘safe’; otherwise, it is classified as ‘warning’. The platform adopts a three-step progressive architecture of intelligent optimisation-adaptive clustering-collaborative decision-making.

First, the algorithm performs image preprocessing on the test strip to convert the probe image into a grey-scale image for subsequent analysis. On this basis, an adaptive threshold segmentation method is used to dynamically adjust the threshold value according to the grey-scale characteristics of the local region, which overcomes the limitations of traditional global threshold segmentation when dealing with different brightness regions. In order to further optimise the segmentation effect, an adaptive threshold segmentation framework based on local contrast perception is proposed, and a dynamic optimisation algorithm in the parameter space is constructed by introducing the ant colony bionic algorithm, which is an intelligent optimisation mechanism of the colony.

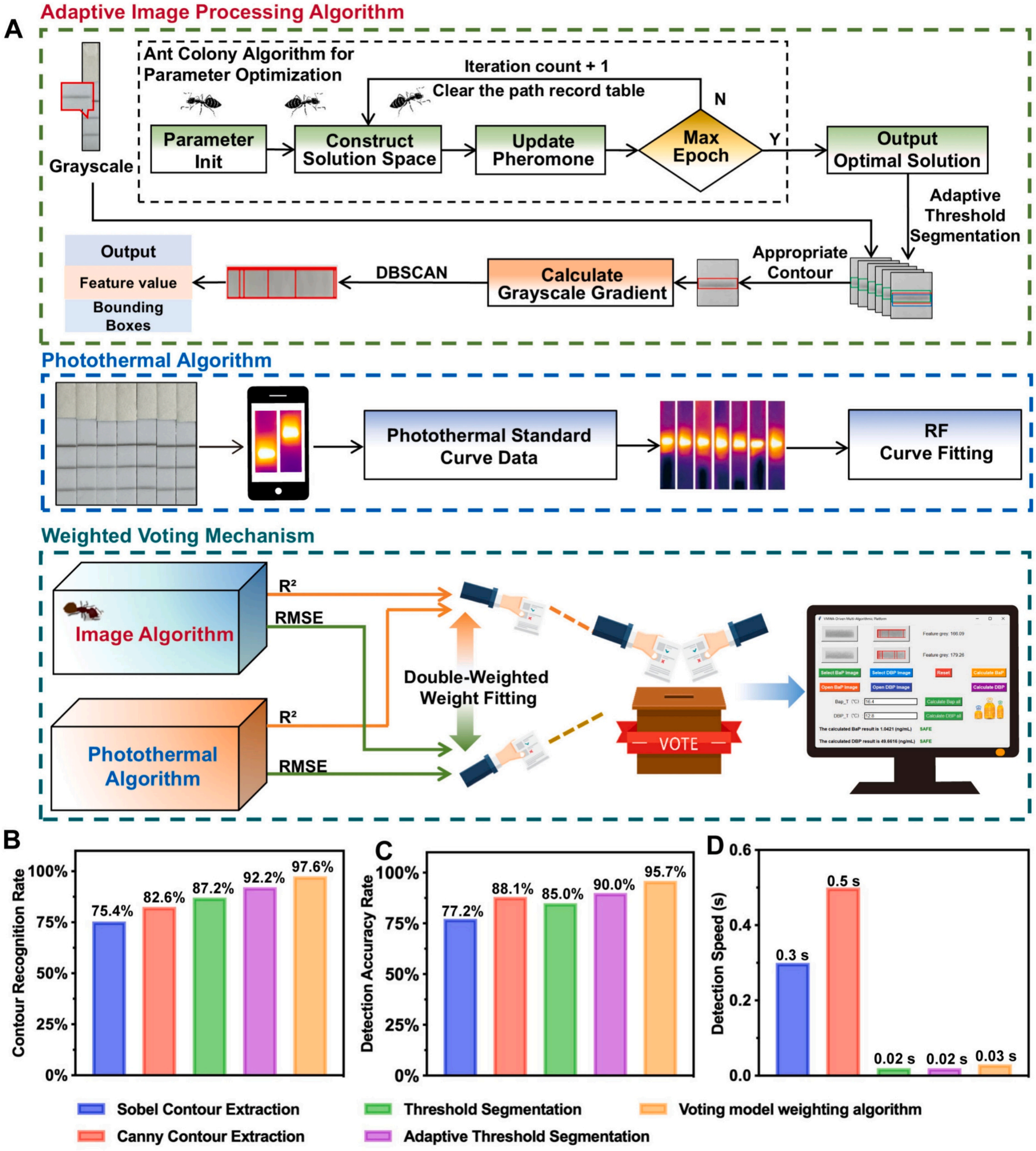

Feature grey: 166.09

Feature grey: 179.26

Bap_T (℃) : 16.4

DBP_T (℃) : 12.8

The calculated BaP result is 1.0421 (ng/mL) SAFE

The calculated DBP result is 49.6616 (ng/mL) SAFE

Fig. 8. Construction and performance analysis of MAPOCT. (A) Schematic Flowchart of VMWA. (B) Contour extraction recognition rate. (C) Algorithm prediction accuracy. (D) Algorithm running speed.

The algorithm simulates the pheromone positive feedback mechanism in the foraging behaviour of ants in nature, transforms the optimization of block size and compensation coefficient (C) into a topological search problem of parameter combination, and guides the virtual ‘ants’ to independently evolve the optimal segmentation strategy in the iteration through the pheromone matrix. After completing the image segmentation, the platform carries out region division and feature extraction. By analyzing the contours, only the region with the largest area is retained, and the area of the smallest external rectangle is used as the evaluation criterion to further improve the accuracy and effectiveness of the segmented region.

Secondly, POCT strips have the problem of uneven grey scale, and simple threshold segmentation and contour extraction are often unable to distinguish different regions finely in images with significant grey scale changes or strong noise. Moreover, the blurring of the boundary of the chromogenic region and noise interference seriously affect the accuracy of BaP and DBP readings. To overcome this challenge, in this study, we introduce the DBSCAN algorithm. The core advantage of the DBSCAN algorithm is that it does not need to set the number of clusters in advance, and is able to automatically identify the clusters of arbitrary shapes, and to detect the noise. The core advantage of the DBSCAN algorithm is that it does not need to set the number of clusters in advance, and can automatically identify clusters of arbitrary shapes and is robust to noise. In the field of image processing, DBSCAN is widely used in image segmentation and feature extraction. The algorithm adaptively divides the image into multiple regions by clustering the gradient of the image grey-scale map and effectively excludes noise points. Specifically, we calculate the gradient value of the image grey-scale map and obtain the grey-scale change information of each pixel point, which is used as the input data of the DBSCAN algorithm. On this basis, the DBSCAN algorithm clusters the grey-scale gradients based on the set parameters of neighbourhood radius (eps) and minimum number of samples (min_samples). In this way, the algorithm is able to automatically discover regions with more consistent grey-scale changes, and effectively screen the regions based on their area and grey-scale uniformity, and finally select the most representative regions for subsequent analysis. In this study, the introduction of the DBSCAN algorithm effectively improves the accuracy and robustness of image segmentation.

Then, after completing the image multi-region semantic segmentation and multi-dimensional feature extraction, this study constructs an intelligent analysis framework based on the collaborative decision-making of heterogeneous models. Aiming at the mapping relationship between the photothermal features of the detected strips and the concentration of the target, a linear regression model was first introduced. Linear regression, as a classical and powerful data analysis tool, can provide preliminary estimation for concentration prediction by establishing a linear mapping relationship between feature values and target concentration. On this basis, the Random Forest integrated learning algorithm is introduced to construct a nonlinear enhanced prediction model. In this study, features extracted based on the photothermal detection algorithm are fed into the Random Forest model, and its implicit feature combination capability is utilised to capture higher-order interaction effects in complex detection environments.

Ultimately, in order to give full play to the complementary advantages of heterogeneous models, this paper proposes a dual-indicator-driven dynamic weight adaptive fusion strategy. The mechanism constructs a multidimensional model performance evaluation system that includes the inverse of the RMSE and the coefficient of determination (R^2), where the RMSE measures the average error between the predicted value and the true value, and the R^2 reflects the degree of model fit to the data. The weight assignment algorithm dynamically adjusts the decision weights of each model by assessing the generalisation performance of the model on the validation set in real time, which effectively solves the environmental adaptability limitation of the traditional static weighting mechanism. The weighted predictions are fused through a common voting mechanism to obtain the optimal quantitative values of BaP and DBP.

In this study, a total of 40 samples of DBP and BaP detection strips with different gradients were prepared, and these samples were respectively subjected to colorimetric quantitative computation based on the traditional contour extraction technique for extracting image contours and using the average grey value of the extracted region as the feature grey value, as well as to quantitative computation using the aforementioned intelligent diagnostic platform for multimodal information fusion, and were respectively evaluated for these algorithms for their contour extraction recognition rate, detection accuracy, and detection speed of these algorithms, and the results are shown in Fig. 8B, C, and D, where the contour extraction recognition rate is evaluated by using the intersection ratio of the extracted contour and the real contour as the evaluation index.

Results demonstrate that the multimodal information fusion intelligent diagnosis platform developed in this study, based on the VMWA, significantly outperforms traditional methods in terms of contour extraction recognition rate, detection accuracy, and detection speed.

Specifically, as shown in Fig. 8B, the contour recognition rates of the traditional Sobel and Canny operators are 75.4 % and 82.6 %, respectively. The lower recognition rates indicate their sensitivity to complex backgrounds and variations in illumination. In contrast, the threshold segmentation method (Threshold Segmentation) and the adaptive threshold segmentation method (Adaptive Threshold Segmentation) show improved contour recognition rates, reaching 87.2 % and 92.2 %, respectively. The VMWA method achieved the highest contour recognition rate of 97.6 %. This advantage is primarily attributed to the ant colony algorithm-optimized adaptive threshold segmentation method. By adjusting the segmentation threshold based on local contrast perception, this method enables the system to adapt to different lighting conditions and effectively removes background noise. The detection performance of MAPOCT was evaluated under different lighting conditions, as shown in Fig. S11. The algorithm demonstrated stable predictive performance when analyzing identical concentrations of DBP and BaP under three illumination environments: outdoor daylight, indoor artificial light, and indoor natural daylight (Fig. S11). The coefficients of variation for DBP and BaP detection were 2.9 % and 3.8 %, respectively, indicating good repeatability and robustness of the MAPOCT system. Moreover, the swarm intelligence optimization mechanism refines the block size and compensation coefficient through dynamic adjustment, further enhancing the precision of contour recognition.

In terms of detection accuracy, the threshold segmentation and adaptive threshold segmentation methods achieved rates of 85.0 % and 90.0 %, respectively (Fig. 8C). The VMWA method further improved the detection accuracy to 95.7 %. This enhancement can be attributed to the following factors: First, the introduction of the DBSCAN enables the detection algorithm to effectively identify and exclude noise points, ensuring the stability of the feature regions. Second, while traditional methods rely solely on global thresholds or fixed edge detection operators, the VMWA method combines adaptive clustering and collaborative decision-making strategies, enabling the self-adjustment of feature extraction methods in different regions and enhancing adaptability to complex backgrounds and low-contrast areas.

Regarding detection speed (Fig. 8D), the Sobel and Canny methods have longer processing times, at 0.5 s and 0.3 s, respectively. This is mainly because these methods require gradient calculations and non-maximum suppression for the entire image when computing edge information, resulting in higher computational complexity. In contrast, the threshold segmentation-based methods significantly improved processing speed, with times of only 0.02 s and 0.03 s. The VMWA method maintains a fast detection speed while achieving high recognition and accuracy rates. This is primarily due to the following optimization strategies: First, the adaptive threshold segmentation reduces global calculations for the entire image, avoiding unnecessary computational overhead; second, the ant colony optimization algorithm accelerates the parameter optimization process, enabling the algorithm to converge to the optimal segmentation strategy within a limited number of iterations.

3.8. Practical application of MAPOCT

To evaluate the sensing performance of POCT in real sample testing and to compare the accuracy of manual readings with MAPOCT results, three of the world's most widely consumed edible oils—palm oil, soybean oil, and rapeseed oil—were selected as test samples. The testing process is depicted in Fig. S12, where edible oil samples were extracted, purified, and subsequently subjected to MAPOCT and instrumental analysis. After extraction and purification, the color of the edible oil samples became significantly lighter compared to the original samples, effectively reducing matrix color interference (Fig. S13). The standard curve for DBP detection by GC–MS was established as Y = 905.1× + 1608 (Fig. S14A), with a retention time of 10.93 min (Fig. S14B). Similarly, the standard curve for BaP detection by HPLC was determined as Y = 2.898× + 0.7834 (Fig. S14C), with a retention time of 7.037 min (Fig. S14D). The spiked concentrations of DBP were 50 ng/mL, 200 ng/mL, and 500 ng/mL, with the results of the three methods presented in Table S4. The recoveries for manual readings of POCT ranged from 92.75 % to 104.84 %, with coefficients of variation (CV) below 7.08 %. For MAPOCT, the recoveries ranged from 94.46 % to 103.46 %, with CVs under 4.89 %. Similarly, the spiked concentrations of BaP were 1 ng/mL, 5 ng/mL, and 20 ng/mL, and the results of the recovery experiments are shown in Table S5. The recoveries for manual readings of POCT ranged from 87.57 % to 94.80 %, with a CV of <6.02 %, while the recoveries predicted by MAPOCT ranged from 90.12 % to 101.91 %, with a CV under 4.61 %. These experiments demonstrated that MAPOCT-predicted results were more accurate and reduced the error associated with manual readings. In addition, to further evaluate the practical performance of the detection platform, we tested nine different types of real edible oil samples (Fig. S15), including palm oil, soybean oil, rapeseed oil, peanut oil, corn oil, sunflower oil, olive oil, sesame oil, and camellia oil. The comparative results obtained from both large-scale instruments and the MAPOCT platform showed that the CVs for DBP and BaP were <3.54 % and 7.80 %, respectively (Table S6). Moreover, the MAPOCT results exhibited strong correlations with those obtained by GC–MS and HPLC, indicating that the platform maintained high detection accuracy and stability across various complex edible oil matrices. These findings confirm that MAPOCT can reliably predict DBP and BaP contents in real-world edible oil samples.

4. Conclusion

In summary, we present a dual-target, dual-mode POCT method based on lateral flow immunoassay and establish a quantitative, MAPOCT employing a voting model weighting algorithm. This method is applied to the simultaneous detection of DBP and BaP in edible oils for early warning purposes. First, photothermal nanomaterial Zn-CN was synthesized via high-temperature pyrolysis of ZIF-8, followed by the loading of platinum nanoparticles to obtain Pt-Zn-CN. The resulting Pt-Zn-CN exhibited a rough and porous surface with a high specific surface area, facilitating antibody coupling and adsorption. The integration of platinum nanoparticles also imparted excellent aqueous dispersibility and enhanced photothermal properties. Subsequently, DBP-mAb@Pt-Zn-CN and BaP-mAb@Pt-Zn-CN probes were prepared through electrostatic coupling of specific monoclonal antibodies with the Pt-Zn-CN. The developed POCT system produced a stable colorimetric signal within 7 min and a stable photothermal signal within 30 s under 808 nm laser excitation. Under both detection modes, the limits of detection were 0.184 ng/mL for DBP and 0.096 ng/mL for BaP, demonstrating high sensitivity and rapid response for early warning. Finally, the MAPOCT platform was developed by integrating a voting model weighting algorithm with adaptive threshold segmentation based on the ant colony algorithm and detection region partitioning via the DBSCAN clustering algorithm. By combining a photothermal detection algorithm with a colorimetric regression model, a weighted voting mechanism was realized. This approach achieved a 97.6 % recognition rate of strip profiles, with an algorithm runtime of only 0.03 s. Leveraging multi-algorithm fusion driven by artificial intelligence, MAPOCT eliminates the need for manual parameter tuning inherent in traditional methods, significantly reduces human reading errors, enhances detection accuracy, and provides a practical solution for the rapid screening of hazardous contaminants in food.

CRediT authorship contribution statement

Zhiqiang Li: Writing – original draft, Visualization, Validation, Methodology, Investigation, Data curation, Conceptualization. **Yating Hu:** Writing – original draft, Software, Methodology, Data curation. **Wen Zhang:** Supervision, Formal analysis. **Qi Zhang:** Supervision, Formal analysis. **Peiwu Li:** Resources, Project administration, Funding acquisition. **Xiaoqian Tang:** Writing – review & editing, Supervision, Funding acquisition, Conceptualization.

Declaration of competing interest

The authors declare that they have no known competing financial interests or personal relationships that could have appeared to influence the work reported in this paper.

Acknowledgements

This work was supported by the National Natural Science Foundation of China (32422072; U22A20551).

Appendix A. Supplementary data

Supplementary data to this article can be found online at https://doi.org/10.1016/j.cej.2025.165872.

Data availability

Data will be made available on request.

References

[1] E. Candellone, A. Aleta, H.F. de Arruda, E. Meijaard, Y. Moreno, Characteristics of the vegetable oil debate in social-media and its implications for sustainability, Commun. Earth Environ. 5 (1) (2024) 10, https://doi.org/10.1038/s43247-024-01545-x.

[2] M.V. Chiriacò, N. Galli, M. Latella, M.C. Rulli, Pressure on global forests: implications of rising vegetable oils consumption under the EAT-lancet diet, Glob. Chang. Biol. 31 (2) (2025) e70077, https://doi.org/10.1111/gcb.70077.

[3] D.S. Mackay, S. Jew, P.J.H. Jones, Best practices for design and implementation of human clinical trials studying dietary oils, Prog. Lipid Res. 65 (2017) 1–11, https://doi.org/10.1016/j.plipres.2016.10.003.

[4] X.R. Zhou, Q. Liu, S. Singh, Engineering nutritionally improved edible plant oils, Annu. Rev. Food Sci. Technol. 14 (2023) 247–269, https://doi.org/10.1146/annurev-food-052720-104852.

[5] L. Shi, L. Zheng, R. Liu, M. Chang, J. Huang, Q. Jin, X. Wang, Quantification of polycyclic aromatic hydrocarbons and phthalic acid esters in deodorizer distillates obtained from soybean, rapeseed, corn and rice bran oils, Food Chem. 275 (2019) 206–213, https://doi.org/10.1016/j.foodchem.2018.09.119.

[6] Y.M. He, W.C. Lin, C. Shi, R.H. Li, C.K. Mu, C.L. Wang, Y.F. Ye, Accumulation, detoxification, and toxicity of dibutyl phthalate in the swimming crab, Chemosphere 289 (2022) 8, https://doi.org/10.1016/j.chemosphere.2021.133183.

[7] H. Wei, X. Yang, L. Cheng, Q. Zhang, J. Mao, P. Li, Simultaneous analysis of PAEs in edible oil and dietary exposure assessment in Hubei, Food Chem. 468 (2025) 142389, https://doi.org/10.1016/j.foodchem.2024.142389.

[8] Y.-R. Liang, Z.-M. Zhang, Z.-J. Liu, K. Wang, X.-Y. Wu, K. Zeng, H. Meng, Z. Zhang, A highly sensitive signal-amplified gold nanoparticle-based electrochemical immunosensor for dibutyl phthalate detection, Biosens. Bioelectron. 91 (2017) 199–202, https://doi.org/10.1016/j.bios.2016.12.007.

[9] H. Chi, C. Li, M. Huang, J. Wan, X. Zhou, B. Yan, Targeted accumulation and spatial confinement effect of Fe(II)-MOFs@MIP for efficiently removing low

concentration dibutyl phthalate, Chem. Eng. J. 424 (2021) 130367, https://doi.org/10.1016/j.cej.2021.130367.

[10] J.M. Ji, M.M. Jiang, Y.X. Zhang, J. Hou, S.D. Sun, Polycyclic aromatic hydrocarbons contamination in edible oils: a review, Food Rev. Int. 39 (9) (2023) 6977–7003, https://doi.org/10.1080/87559129.2022.2131816.

[11] C.M. Sánchez-Arévalo, L. Olmo-García, J.F. Fernández-Sánchez, A. Carrasco-Pancorbo, Polycyclic aromatic hydrocarbons in edible oils: an overview on sample preparation, determination strategies, and relative abundance of prevalent compounds, Compr. Rev. Food Sci. Food Saf. 19 (6) (2020) 3528–3573, https://doi.org/10.1111/1541-4337.12637.

[12] J. Pan, G. Wang, J. Nong, Q. Xie, Biodegradation of benzo(a)pyrene by a genetically engineered Bacillus licheniformis: degradation, metabolic pathway and toxicity analysis, Chem. Eng. J. 478 (2023) 147478, https://doi.org/10.1016/j.cej.2023.147478.

[13] J. Ma, X.L. Liu, Y. Yang, J.H. Qiu, Z. Dong, Q.Z. Ren, Y.Y. Zuo, T. Xia, W. Chen, S. J. Liu, Binding of benzo(a)pyrene alters the bioreactivity of fine biochar particles toward macrophages leading to deregulated macrophagic defense and autophagy, ACS Nano 15 (6) (2021) 9717–9731, https://doi.org/10.1021/acsnano.1c00324.

[14] X. Zou, Q. Su, Q. Yi, L. Guo, D. Chen, B. Wang, Y. Li, J. Li, Determining the degradation mechanism and application potential of benzopyrene-degrading bacterium Acinetobacter XS-4 by screening, J. Hazard. Mater. 456 (2023) 131666, https://doi.org/10.1016/j.jhazmat.2023.131666.

[15] L. Xi, Y. Shang, Z. Wang, J. Wang, Q. Wu, Y. Shen, Y. Ding, Programmable DNA hydrogels for biosensing and point-of-care test, Coord. Chem. Rev. 518 (2024) 216084, https://doi.org/10.1016/j.ccr.2024.216084.

[16] S. Rink, A.J. Baeumner, Progression of paper-based point-of-care testing toward being an indispensable diagnostic tool in future healthcare, Anal. Chem. 95 (3) (2023) 1785–1793, https://doi.org/10.1021/acs.analchem.2c04442.

[17] C. Wang, C. Xiang, H. Zhang, G. Zhang, Q. Zhang, P. Li, X. Tang, Multifunctional metal-organic frameworks-mediated colorimetric/photothermal immunosensor for highly sensitivity detection of dibutyl phthalate, Food Chem. 472 (2025) 142928, https://doi.org/10.1016/j.foodchem.2025.142928.

[18] X. Chen, W.Q. Wu, J. Zeng, E. Ibañez, A. Cifuentes, J. Mao, L. Yu, H.M. Wu, P.W. Li, Z.W. Zhang, A smartphone-powered photoelectrochemical POCT via Z-scheme Cu2O/Cu3SnS4 for dibutyl phthalate in the environmental and food, J. Hazard. Mater. 460 (2023) 10, https://doi.org/10.1016/j.jhazmat.2023.132281.

[19] Y. Zhao, W. Wu, X. Tang, Q. Zhang, J. Mao, L. Yu, P. Li, Z. Zhang, A universal CRISPR/Cas12a-powered intelligent point-of-care testing platform for multiple small molecules in the healthcare, environment, and food, Biosens. Bioelectron. 225 (2023) 115102, https://doi.org/10.1016/j.bios.2023.115102.

[20] Y. Wang, Y. Rong, T. Ma, L. Li, X. Li, P. Zhu, S. Zhou, J. Yu, Y. Zhang, Photoelectrochemical sensors based on paper and their emerging applications in point-of-care testing, Biosens. Bioelectron. 236 (2023) 115400, https://doi.org/10.1016/j.bios.2023.115400.

[21] S. Lee, L. Bi, H. Chen, D. Lin, R. Mei, Y. Wu, L. Chen, S.-W. Joo, J. Choo, Recent advances in point-of-care testing of COVID-19, Chem. Soc. Rev. 52 (24) (2023) 8500–8530, https://doi.org/10.1039/D3CS00709J.

[22] X. Yin, S. Liu, D. Kukkar, J. Wang, D. Zhang, K.-H. Kim, Performance enhancement of the lateral flow immunoassay by use of composite nanoparticles as signal labels, TrAC Trends Anal. Chem. 170 (2024) 117441, https://doi.org/10.1016/j.trac.2023.117441.

[23] S. Liu, Y. Liao, R. Shu, J. Sun, D. Zhang, W. Zhang, J. Wang, Evaluation of the multidimensional enhanced lateral flow immunoassay in point-of-care nanosensors, ACS Nano 18 (40) (2024) 27167–27205, https://doi.org/10.1021/acsnano.4c06564.

[24] R. Archana, P.S.E. Jeevaraj, Deep learning models for digital image processing: a review, Artif. Intell. Rev. 57 (1) (2024) 33, https://doi.org/10.1007/s10462-023-10631-z.

[25] M.R. Amin, M. Hasan, M. Degiorgio, Digital image processing to detect adaptive evolution, Mol. Biol. Evol. 41 (12) (2024) 30, https://doi.org/10.1093/molbev/msae242.

[26] P. Vashishtha, H.G. Kattamuri, N. Thawari, M. Amirthalingam, R. Batra, Reusability report: deep learning-based analysis of images and spectroscopy data with AtomAI, Nat. Mach. Intell. 7 (1) (2025) 7, https://doi.org/10.1038/s42256-024-00958-9.

[27] C. Stringer, M. Pachitariu, Cellpose3: one-click image restoration for improved cellular segmentation, Nat. Methods 26 (2025), https://doi.org/10.1038/s41592-025-02595-5.

[28] Ç. Isil, T.Y. Gan, F.O. Ardic, K. Mentesoglu, J. Digani, H. Karaca, H.L. Chen, J.X. Li, D. Mengu, M. Jarrahi, K. Aksit, A. Ozcan, All-optical image denoising using a diffractive visual processor, Light-Sci. Appl. 13 (1) (2024) 17, https://doi.org/10.1038/s41377-024-01385-6.

[29] F. Yan, H.S. Huang, W. Pedrycz, K. Hirota, Review of medical image processing using quantum-enabled algorithms, Artif. Intell. Rev. 57 (11) (2024) 52, https://doi.org/10.1007/s10462-024-10932-x.

[30] S. Miron, J. Flamant, N. Le Bihan, P. Chainais, D. Brie, Quaternions in signal and image processing: a comprehensive and objective overview, IEEE Signal Process. Mag. 40 (6) (2023) 26–40, https://doi.org/10.1109/msp.2023.3278071.

[31] C.W. Choi, D. Hong, M.-G. Kim, Light source-free smartphone detection of salivary cortisol via colorimetric lateral flow immunoassay using a photoluminescent film, Biosens. Bioelectron. 271 (2025) 116971, https://doi.org/10.1016/j.bios.2024.116971.

[32] A.D. Beggs, L.A. Consortium, Machine learning for determining lateral flow device results for testing of SARS-CoV-2 infection in asymptomatic populations, Cell Rep. Med. 3 (10) (2022) 11, https://doi.org/10.1016/j.xcrm.2022.100784.

[33] H.Y. Tong, C.Y. Cao, M.L. You, S. Han, Z. Liu, Y. Xiao, W.H. He, C. Liu, P. Peng, Z. R. Xue, Y. Gong, C.Y. Yao, F. Xu, Artificial intelligence-assisted colorimetric lateral flow immunoassay for sensitive and quantitative detection of COVID-19 neutralizing antibody, Biosens. Bioelectron. 213 (2022), https://doi.org/10.1016/j.bios.2022.114449.

[34] S. Lee, J.S. Park, H. Woo, Y.K. Yoo, D. Lee, S. Chung, D.S. Yoon, K.B. Lee, J.H. Lee, Rapid deep learning-assisted predictive diagnostics for point-of-care testing, Nat. Commun. 15 (1) (2024) 12, https://doi.org/10.1038/s41467-024-46069-2.

[35] Y. Zhu, L. Ao, S. Chu, Y. Liao, J. Wang, J. Hu, L. Huang, Semiconductor nanoplatelets based host-guest assembly structure with high color purity for hue-recognizable lateral flow immunoassay, Adv. Funct. Mater. 34 (26) (2024) 2316147, https://doi.org/10.1002/adfm.202316147.

[36] Y. Zha, Y. Li, J. Zhou, X. Liu, K.S. Park, Y. Zhou, Dual-mode fluorescent/intelligent lateral flow immunoassay based on machine learning algorithm for ultrasensitive analysis of chloroacetamide herbicides, Anal. Chem. 96 (29) (2024) 12197–12204, https://doi.org/10.1021/acs.analchem.4c02500.

[37] X. Zhang, H. Zhi, F. Wang, M. Zhu, H. Meng, P. Wan, L. Feng, Target-responsive smart nanomaterials via a Au–S binding encapsulation strategy for electrochemical/colorimetric dual-mode paper-based analytical devices, Anal. Chem. 94 (5) (2022) 2569–2577, https://doi.org/10.1021/acs.analchem.1c04537.

[38] Z. Li, W. Zhang, Q. Zhang, P. Li, X. Tang, Self-assembly multivalent fluorescence-nanobody coupled multifunctional nanomaterial with colorimetric fluorescence and photothermal to enhance immunochromatographic assay, ACS Nano 17 (19) (2023) 19359–19371, https://doi.org/10.1021/acsnano.3c06930.

[39] X. Wang, X. Sun, T. Bu, Q. Wang, P. Jia, M. Dong, L. Wang, In situ fabrication of metal-organic framework derived hybrid nanozymes for enhanced nanozyme-photothermal therapy of bacteria-infected wounds, Compos. Part B Eng. 229 (2022) 109465, https://doi.org/10.1016/j.compositesb.2021.109465.

[40] W. Chen, C. Liu, X.Y. Ji, J. Joseph, Z.M. Tang, J. Ouyang, Y.F. Xiao, N. Kong, N. Joshi, O.C. Farokhzad, W. Tao, T. Xie, Stanene-based nanosheets for β-elemene delivery and ultrasound-mediated combination cancer therapy, Angew. Chem.-Int. Edit. 60 (13) (2021) 7155–7164, https://doi.org/10.1002/anie.202016330.

[41] H.B. Dong, S.H. Zhang, L.G. Yang, N. Wang, S.J. Chen, J.W. Ma, J.W. Li, Cu/Zn galvanic couples composite antibacterial dressings prepared by template-assisted magnetron sputtering, Compos. Part B-Eng. 224 (2021) 8, https://doi.org/10.1016/j.compositesb.2021.109240.